Impact of magnetic and antisite disorder on the vibrational densities of states in math xmlns="http://www.w3.org/1998/Math/MathML">msub>mi mathvariant="normal">Ni/mi>mn>2/mn>/msub>mi>MnSn/mi>/math> Heusler alloys

Olga N. Miroshkina, Benedikt Eggert, Johanna Lill, Benedikt Beckmann, David Koch, Michael Y. Hu, Tobias Lojewski, Simon Rauls, Franziska Scheibel, Andreas Taubel, Mojmir Šob, Katharina Ollefs, Oliver Gutfleisch, Heiko Wende, Markus E. Gruner, and Martin Friák

Impact of magnetic and anti-site disorder on the vibrational densities of states in Ni$_2$MnSn Heusler alloys

Olga N. Miroshkina[1,∥],[*] Benedikt Eggert[1,∥], Johanna Lill[1], Benedikt Beckmann[2], David Koch[2],
Michael Y. Hu[3], Tobias Lojewski[1], Simon Rauls[1], Franziska Scheibel[2], Andreas Taubel[2], Mojmír
Šob[4,5], Katharina Ollefs[1], Oliver Gutfleisch[2], Heiko Wende[1], Markus E. Gruner[1], and Martin Friák[5]

[1] *Faculty of Physics and Center for Nanointegration Duisburg-Essen (CENIDE),*
University of Duisburg-Essen, 47057 Duisburg, Germany
[2] *Institute of Materials Science, Technical University of Darmstadt, 64287 Darmstadt, Germany*
[3] *Advanced Photon Source (APS), Argonne National Laboratory, Lemont, IL 60439, USA*
[4] *Department of Chemistry, Faculty of Science, Masaryk University,*
Kotlářská 2, CZ-611 37 Brno, Czech Republic and
[5] *Institute of Physics of Materials, v.v.i., Czech Academy of Sciences, Žižkova 22, CZ-616 62 Brno, Czech Republic*
(Dated: November 15, 2022)

We have performed a combined experimental and theoretical investigation of the vibrational properties of Ni$_2$MnSn Heusler alloys. Sn-partial vibrational density of states (VDOS) of ^{119}Sn was measured by nuclear resonant inelastic x-ray scattering (NRIXS) at temperatures of 15 K and 300 K, while magnetism and local environment of Sn was resolved by ^{119}Sn Mössbauer spectroscopy. Using density functional theory, we associate the peaks in the VDOS with particular features in the element-resolved phonon dispersion of L2$_1$ ordered Ni$_2$MnSn. The good agreement between theory and experiment in the low-energy region provides the evidence that the inversion of optical modes at Γ involving the displacement of Ni and the heavier main group element atoms, which was predicted previously for other Ni-Mn-based Heusler compounds, is also a characteristic property of Ni$_2$MnSn. Introducing different types of magnetic and anti-site disorder in our calculations results in a distinctive redistribution and broadening of the Sn-VDOS, suggesting that considering partial disorder further improves the agreement with the experiment in particular at the highest phonon energies.

PACS numbers:

I. INTRODUCTION

Heusler alloys represent one of the most interesting families of materials with many chemical compositions and properties[1]. In particular, the Ni-Mn-based ternary systems, the properties of which were studied both experimentally[2–11] and theoretically[11–17], exhibit magnetic shape memory effect[18], magnetic superelasticity[19] or barocaloric and magnetocaloric effects[20–22]. As strong coupling effects in magnetocaloric materials are the key factor to achieve a large magnetic entropy change, Waske *et al.*[23] recently compiled results for atomic, stress, and magnetostatic coupling in a set of Heusler compounds including Mn-rich Ni-Mn-Z (Z = Al, In, Sn, Sb).

Our study is focused on the stoichiometric Ni$_2$MnSn that crystallizes in the cubic $Fm\overline{3}m$ structure (L2$_1$, so-called full Heusler phase), which, unlike Mn-rich or Co-doped[24] off-stoichiometric alloys, does not undergo a structural phase transition (see, e.g., Ref. 18). Structural, elastic, electronic, and magnetic properties were computed by, for example, Benguerine *et al.*[25] who compared them with those of Ni$_2$MnSb and Ni$_2$MnSb$_{0.5}$Sn$_{0.5}$ magnetic shape memory alloys and found an increase of total magnetization in the Ni$_2$MnSb$_{0.5}$Sn$_{0.5}$ composition with respect to the stoichiometric ones.

As another example, our recent study of the stoichiometric Ni$_2$MnSn, see Ref. 26, focused on pressure-induced changes in magnetism. Significantly different magnetic states were found in (i) Ni$_2$MnSn containing pairs of swapped atoms (Mn↔Sn, Mn↔Ni, and Ni↔Sn) and (ii) a variety of ferrimagnetic (FiM) states while the associated energy changes were quite small when compared with the energy of the defect-free Ni$_2$MnSn. First reports of the electronic structure and magnetism of stoichiometric Ni$_2$MnSn from density functional theory (DFT) date back to the work of Kübler, Williams and Sommer[27]. Later on, it was pointed out that – similarly to the other Ni-Mn-based compounds – Mn atoms on comparatively close next-nearest neighbor positions tend to develop a rather strong antiferromagnetic coupling already in the cubic phase[17]. This induces inhomogeneous magnetic arrangements in off-stoichiometric and disordered alloys leading eventually to an effective magnetic decoupling of different sublattices containing Mn (Ref. 28).

As a part of nanocomposites, Ni$_2$MnSn was studied by Dutta, Opahle, and Hickel[29], who calculated and analyzed interface effects on the magnetic properties of layered Ni$_2$MnGa/Ni$_2$MnSn nanocomposite alloys. The authors found that (i) the Ni spin moments at the interface changed by about 30 % compared to the bulk value, and (ii) the magneto-crystalline anisotropy of the multilayer systems can be understood by the additive contributions of the respective strained bulk phases.

Our current study is focused on vibrational properties of Ni$_2$MnSn and it was partly motivated by previous findings published in literature. For example, phonon spectrum was computed by the density functional per-

turbation theory (DFPT) for the defect-free Ni_2MnSn in Ref. 30 and compared with that of Ni_2MnSb. The total phonon densities of states of both compounds exhibit similar features, but some imaginary phonon frequencies in the case of Ni_2MnSb render it mechanically unstable, in contrast to the stability of Ni_2MnSn. Recarte *et al.* determined the contribution from vibrational entropy to the entropy change at the phase transition in off-stoichiometric Ni-Mn-Sn by time-of-flight neutron spectroscopy[31]. Their estimate is based on neutron weighting correction was obtained from DFT calculations of the phonon VDOS of the stoichiometric Ni_2MnSn.

Regarding phonon calculations in Ni_2MnSn with point defects (or disordered Ni-Mn-Sn systems in general), theoretical studies based on supercell calculations are rare. This lack of theoretical results stems from the facts that (i) computational models of disordered systems use supercells with a large number of atoms, (ii) the symmetry of disordered systems is typically very low, (iii) determination of phonon spectra requires calculations of multiple finite displacements for all atoms not related by symmetry operations, and (iv) topological disorder in the form of internal twinning or modulation in the low-temperature martensite phase further complicates the phonon evaluation. As an example, phonons calculated for off-stoichiometric FiM disordered $Ni_{31}Mn_{25}Sn_8$ martensite modeled by a 64-atom orthorhombic supercell were recently published in Ref. 32. The system was found mechanically stable, i.e. without any imaginary phonon frequencies. Regarding electronic and magnetic properties, magnetic moments of atoms were found to sensitively depend on their local crystal environment.

In this work, we present a combined experimental and theoretical study of vibrational properties in Ni_2MnSn focusing on Sn atoms. To improve the matching between the DFT calculated and obtained by ^{119}Sn-NRIXS high-energy part of Sn-partial VDOS in the defect-free Ni_2MnSn, we have computed phonon spectra also for Ni_2MnSn with chemical and magnetic disorder, the presence of which was confirmed by Mössbauer spectroscopy. In our calculations, the disorder was modeled in terms of Mn↔Ni and Mn↔Sn anti-site swaps and reversed magnetic moments. This results in redistribution of the Sn-VDOS and broadening of the energy level providing a better agreement with experimental findings.

This paper is organised as follows. Section II is devoted to the description of experimental techniques and computational methods used for simulations. Section III presents results and discussion of the Sn-partial VDOS study at low and room temperature (Sec. III A), site-resolved phonon dispersion of L2$_1$ Ni_2MnSn (Sec. III B) as well as the analysis of the anti-site and magnetic disorder effect on site distribution of the partial magnetic moments (Sec. III C) and total and partial VDOS (Sec. III D). Important conclusions and final remarks are summarized in Sec. IV. Systematic testing of the potentials used for quantum-mechanical calculations is presented in the Appendix.

II. TECHNICAL DETAILS

A. Experiment

The Ni_2MnSn sample was prepared by arc melting of pure elements (Ni: 99.97 %, Mn: 99.8 %, Sn: 99.999 %), using 4 % Mn excess to counter evaporation losses. The polycrystalline ingot has been encapsulated and annealed in a quartz tube under Ar atmosphere at 1273 K for 24 h, followed by quenching in room temperature water. The 6-gram sample was turned and remolten seven times to ensure a homogeneous element distribution. Energy-dispersive x-ray spectroscopy (EDX), using a Tescan Vega3 scanning electron microscope (SEM), and inductively coupled plasma optical emission spectroscopy (ICP-OES), using a Thermo Fisher Scientific iCAP PRO XP-Duo, verifies the composition of the prepared alloy to be $Ni_{49.1}Mn_{24.7}Sn_{26.2}$. In order to perform x-ray diffraction and ^{119}Sn-Mössbauer spectroscopy, the annealed polycrystalline ingot has been milled to powder (particle size below 100 μm) and further annealed for 15 minutes at 1273 K to reduce mechanical stress, induced during powder milling. We performed ^{119}Sn-Mössbauer spectroscopy to investigate the Sn-partial electronic and magnetic structure. Temperature-dependent measurements were performed in transmission geometry under zero-field conditions in a closed-cycle He cryostat. We used the KETEK AXAS-M solid state detector for signal detection, while only photons with an energy of 23.88 keV $\pm$ 200 eV have been considered. The velocity of a $Ca^{119}SnO_3$ source was changed within the constant-acceleration mode. Experimental spectra were analyzed with the help of a least-squares fitting routine included in the Pi program package[33].

Nuclear resonant inelastic x-ray scattering experiments were performed at the beamline 30-ID of the Advanced Photon Source[34], Argonne National Laboratory. To obtain the ^{119}Sn-partial phonon spectrum, a high-resolution monochromator[35,36] was used in order to tune the energy of the x-ray beam around the ^{119}Sn nuclear resonance energy of 23.88 keV with an energetic bandwith ΔE of 1 meV. For the measurement, the x-ray beam size was 0.4×1.8 mm^2 (V×H), while the measurements were performed in grazing incidence relative to the sample of size 10×10 mm^2. A Ni_2MnSn sample has been attached to the end of a copper post connected to a closed-cycle cryostat. Measurements were conducted at temperatures of 15 K and 300 K. An avalanche photodiode (APD) was used to detect the delayed incoherent inelastic signal by measuring the fluorescence radiation. For a detailed introduction to NRIXS and the corresponding data evaluation, we refer the reader to Refs. 37–39 or to the Supplemental Material (SM)[40], which additionally includes Refs. 41–55. In the present case, the ^{119}Sn-partial VDOS were obtained from the NRIXS spectra employing the PHOENIX[45,46], SciPhon[39], and the Pi[33] software packages. Due to the large absorption, it was necessary to apply the transmission integral[56] for the evaluation of
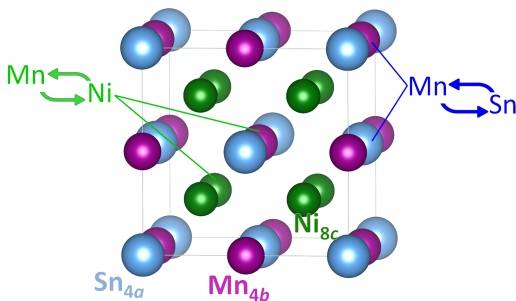
FIG. 1: The computational cell of Ni_2MnSn. In the ideal $L2_1$ structure (space group $Fm\overline{3}m$, No. 225, prototype Cu_2MnAl), we introduce two variants of anti-site disorder: swapping between (i) Mn and Ni (green arrows) and (ii) Mn and Sn (blue arrows). For each case, we modeled ferromagnetic (FM) and FiM ordering. In FM case, all the Mn magnetic moments align parallel, while in the FiM case, the magnetic moment of one Mn atom (the swapped one in the disordered structures) has an antiparallel orientation.

the spectra.

B. Quantum-mechanical calculations

Our first-principles calculations were performed in the framework of DFT using the Vienna *ab initio* simulation package[57] (VASP), which employs a plane-wave basis set in combination with the projector augmented wave (PAW) method[58]. We employed PAW potentials with the following valence states: $3p^6 3d^8 4s^2$ for Ni, $3p^6 3d^5 4s^2$ for Mn and $4d^{10} 5s^2 5p^2$ for Sn. The energy cut-off for plane wave basis set was set to 460 eV. For the exchange and correlation functional, the generalized gradient approximation (GGA) in the Perdew, Burke, and Ernzerhof (PBE) scheme[59] was applied. While perfectly ordered $L2_1$ Ni_2MnSn may be represented in a 4-atom cell with 3 inequivalent Wyckoff positions, i. e., Ni on ($8c$), Sn on ($4a$) and Mn on ($4b$), we used the 16 atom supercell shown in Fig. 1 to model disordered configurations which might be present in the experimental samples. In particular, we swapped pairs of (i) Mn and Sn and (ii) Mn and Ni as shown in Fig. 1 by the blue an green arrows, respectively. Furthermore, for $L2_1$ and disordered structures, we considered antiferromagnetic alignment of one Mn magnetic moment (in case of disordered structures – the moment of swapped Mn atom) to simulate FiM systems.

For all these systems, a full structural relaxation with respect to lattice parameters and ionic-position was performed. For the Brillouin zone integration we used a uniform Monkhorst-Pack $13 \times 13 \times 13$ k-point mesh using the first-order Methfessel-Paxton method with a smearing parameter of 0.1 eV. Calculations of the VDOS were performed in the harmonic approximation within the direct (force-constant) method using Phonopy[60] package. Here, Hellmann–Feynman forces were obtained from a set

of non-equivalent atomic displacements of 0.02 Å of the inequivalent ions in $2 \times 2 \times 2$ (128 atoms) supercells with $4 \times 4 \times 4$ k-mesh. The calculated forces allow to construct the force constant matrix of the system and the evaluation of eigenvalues of the resulting dynamical matrix leads to the VDOS. The phonon band structure was obtained with the help of a 500-atom supercell ($5 \times 5 \times 5$ multiplication of the 4-atom cell) on a $2 \times 2 \times 2$ k-mesh. Here, we used the PHON code[61], to obtain the decomposition of the eigenvectors into the elemental contributions from an interpolation on a $61 \times 61 \times 61$ q-point grid.

III. RESULTS AND DISCUSSION

A. Sn-partial VDOS at low and room temperature

To obtain the Sn-partial VDOS of Ni_2MnSn, we performed [119]Sn NRIXS in the regime of zero-point vibrations ($T = 15$ K) and at room temperature. With NRIXS, we perform a Mössbauer resonance line's incoherent and inelastic scattering process. Due to the incoherent nature of the scattering process, we do not obtain k-dependent insights into the phonon band structure. However, we gain the k-integrated isotope-specific lattice dynamics. For this alloy, [119]Sn is the only suitable isotope to perform such a study due to the low recoil energy of [119]Sn, relatively low resonance energy, and the availability of high-resolution monochromators in this energy regime. Furthermore, the presence of high-resolution monochromators, at this specific photon energies[35,36], makes it possible to obtain the required resolution in the energy domain (in this case $\frac{E}{\Delta E} = 2.4 \times 10^7$) to precisely probe the lattice dynamics.

The actual experimental data and motivation for the process of extracting the VDOS $g(E)$ after (i) subtracting the zero-phonon (Mössbauer) contribution and (ii) normalising the experimental spectra may be found in the SM[40]. Figure 2 illustrates the Sn-partial VDOS $g(E)$ at these two temperatures. At the lower temperature, the Sn-partial VDOS exhibits dominant contributions at 10 meV, 13 meV, 25 meV and 28.5 meV. The low energy contribution can be assigned to Sn-dominated vibrations, while the contributions at higher phonon energies might be due to hybridisation with Mn and Ni. The assignment of these contributions to distinct branches in the phonon band structure will be discussed below.

The comparison of low temperature and room temperature VDOS shows two noticeable effects. At higher phonon energies, we observe a softening of the VDOS that can be explained by thermal expansion of the lattice, leading to an energy reduction $\frac{\Delta E}{E} \approx 1.4\,\%$. The comparison of VDOS measured at low and room temperature points out an intensity reduction in $g(E)$, that is well pronounced at the previously discussed contribution (e.g. at phonon energies E of 10 meV and 28.5 meV). Such a reduction may be due to magnetoelastic coupling and reduced magnetisation. The reduced magnetisation

can be explained by the proximity to the Curie temperature $T_C \approx 340\,\mathrm{K}$, while later effects of magnetic disorder will be discussed later.

B. Site-resolved phonon dispersion of the L2$_1$ ordered compound

A microscopic understanding of the role of the particular features in the Sn-resolved VDOS can be obtained from a comparison of the measured partial VDOS with theoretical element resolved phonon band structure. In contrast to neutron diffraction and NRIXS experiments, DFT calculations of phonons allow to obtain in addition the phonon dispersion resolved with respect to the contribution from each element at each point in reciprocal space. Both are presented in Fig. 3. The phonon bands are color-coded with the primary colors referring to pure-element contributions to a particular phonon mode. The mixed colors indicate contributions from two or even all three elements. Since the latter are difficult to quantify, we additionally plot the contribution of the Sn-subsystem, that is particularly relevant for our discussion. We do so in the form of black vertical lines with the length proportional to the vibration amplitude of the Sn ions. The right hand side of Fig. 3 displays the total and partial VDOS corresponding to all constituents. The shape of the total VDOS and the dispersion lines along Γ-X and K-Γ agree well with previous reports based on DFT calculations within the GGA[30,31]. Similarly well captured is the incomplete softening of the transversal acoustic TA$_2$ mode along the K-Γ direction.

Generally, one expects phonon frequencies to scale inversely with the square root of the mass of the ions.
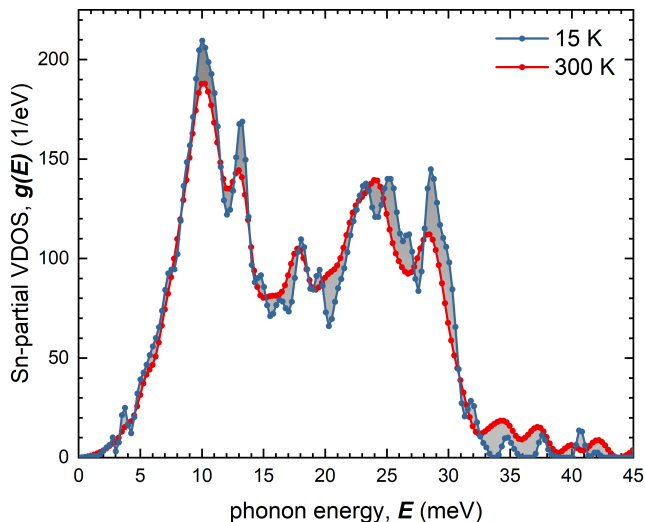

FIG. 2: Experimental Sn-partial VDOS of Ni$_2$MnSn at low temperatures (blue line) and room temperature (red line). The grey-shaded area highlights the difference between the Sn-partial VDOS obtained at these two temperatures.

The heaviest element, Sn, should thus dominate the low frequency end of the spectrum. This is indeed the case for energies below 13 meV. We observe a similarly strong contributions from Ni, which contributes twice in terms of atomic composition and to a comparable amount in terms of wt-%. In contrast, we see almost no contribution from Mn-vibrations to the acoustical modes. Above 13 meV, the VDOS is essentially dominated by Ni. The peaks in this range originate from almost dispersion-less bands with nearly pure Ni character (green color in the dispersion), while for other bands, the yellow color indicates increasing Mn-character. Above 18 meV we encounter first bands with predominant Mn character, while above 23 meV the VDOS is characterized by contributions from all three constituents, which appear almost equal in magnitude. The large amount of admixed, non-primary colors in the rather dispersion-less dispersion and the fact, that the fine structure of the strong peaks in the partial VDOS above 25 meV agrees between the elements speaks in favor of a strong coupling of individual displacements, indicating that a collective motion with similar contribution from all elements characterizes the top end of the spectrum.

The situation, that the Ni vibrations vastly dominate the central part of the vibrational spectrum between 15 and 18 meV, while significantly larger contributions of the heavier atom are found at the top end is present in practically all Ni-Mn-based Heusler alloys. This was consequently termed *mode inversion*[62,63] and discussed in the context of the soft TA$_2$-mode along Γ-K, which is associated with a Kohn anomaly arising from nesting parallel Fermi-surface sheets, separated by the reciprocal vector of the anomaly[64–68]. In the prototypical compound Ni$_2$MnGa, this leads to imaginary modes in the TA$_2$ branch[66,69,70] and eventually to the evolution of modulated martensites[71–74]. These are prerequisites for the giant magnetic shape memory effect observed in this compound[75,76]. Indeed the Fermi surface of Ni$_2$MnSn obtained from DFT exhibits a similar three dimensional structure with nearly parallel, but slightly more corrugated Fermi-surface sheets[77]. These areas are apparently connected along the [110] direction by a larger reciprocal vector as compared to Ni$_2$MnGa, which corroborates the link between the Kohn anomaly and the softening of the TA$_2$ branch appearing at about 80 % of the distance Γ-K in Ni$_2$MnSn.

Following the discussion of Zayak *et al.*[62,63], the mode inversion contributes to this softening, as it brings down a triply degenerate optical mode at Γ with T_{2g} symmetry, which only involves displacements of Ni atoms. In Fig. 3, a corresponding feature can be found at 16.4 meV. In this vibration (111) planes of Ni slide against each other in $[1\bar{1}0]$ direction. This is however incompatible with the displacements along $[1\bar{1}0]$ which are modulated in the TA$_2$ mode along the [110] direction Γ-K, which requires both modes to repel each other[78]. Away from Γ the T_{2g} mode splits up and the decreasing branches potentially push the TA$_2$ mode further down to lower energies.
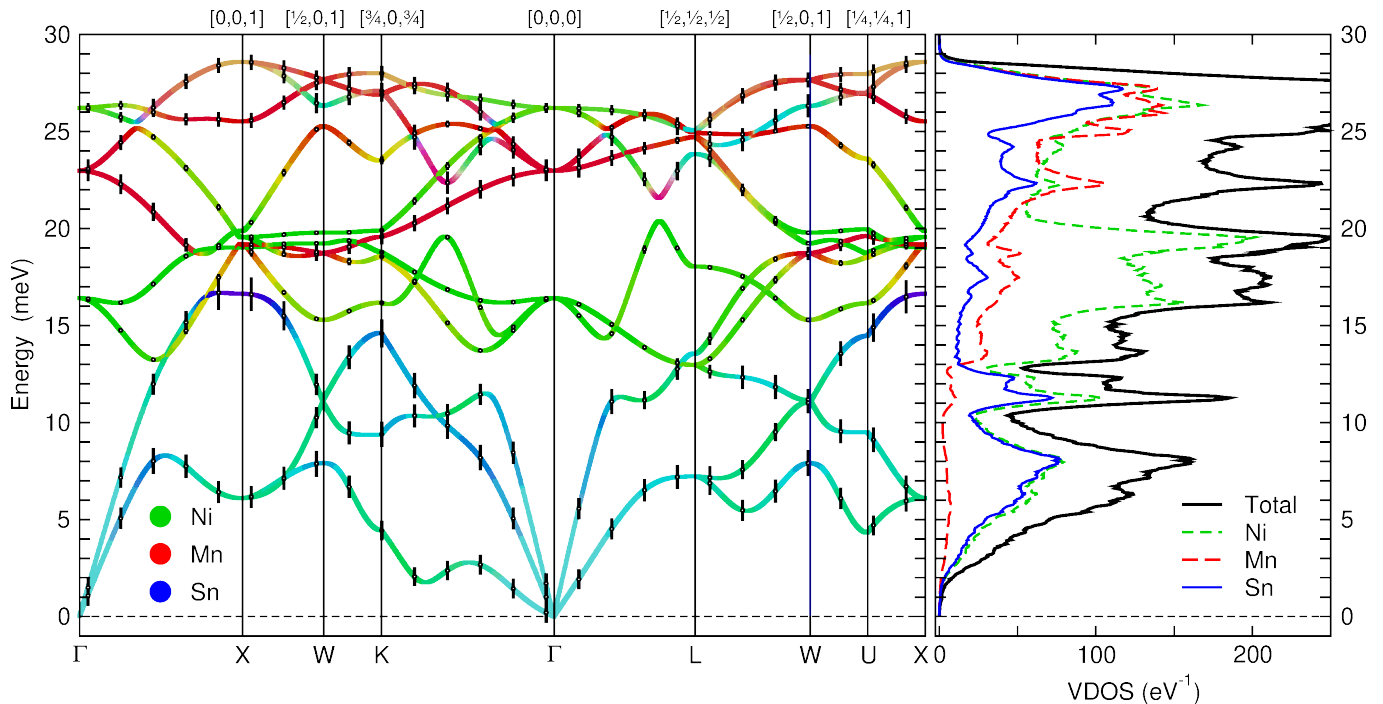
FIG. 3: Phonon band structure (left panel) and corresponding element-resolved VDOS (right panel) of L2$_1$-ordered Ni$_2$MnSn obtained from DFT. The vertical bars plotted on top of the phonon dispersion are proportional to the amplitude of Sn displacements obtained from the eigenvector of the respective mode in reciprocal space. The predominant elemental contributions to each phonon band calculated from the eigenvectors is visualized by the color of the bands (green for Ni, red for Mn, blue for Sn, mixed colors indicate combined contributions).

In contrast, Co$_2$Ni-based Heusler compounds neither exhibit mode inversion in terms of an anomalously low T$_{2g}$ mode nor a softening of the TA$_2$ branch[62]. Apart from K-Γ, Fig. 3 also reveals an indication of an avoided crossing between this T$_{2g}$ mode and both TA modes along Γ-X, which are pushed down to 6 meV at X.

Next we compare the features in the Sn-resolved VDOS from theory and experiment using the site-resolved phonon band structure. As the low-lying TA modes along K-Γ and around X involve the motion of both Ni and Sn atoms, they provide additional weight to the low-energy spectrum of Sn, which are visible as an initial linear increase at lowest energies and a tiny bump around 6 meV. A feature corresponding to the latter might also be tentatively retrieved in the experimental VDOS (Fig. 2), but 6 meV are still too close to the bright central elastic peak to allow for a final conclusion here. In contrast, the next two peaks in experiment (around 10 and 13 meV) can be safely identified with the peaks at 8 and 11 meV in Fig. 3. The lower peak is associated with maxima of the TA modes at L, W and along Γ-X with significant Sn-contribution, while the second peak coincides with the bending of the longitudinal acoustic LA mode along Γ-K and Γ-L, which suggests that this occurs in a larger part of the Brillouin zone as well, giving rise to such a pronounced peak.

In the experimental VDOS, we observe a minor peak at 18 meV which corresponds to a small feature around 17 meV in Fig. 3. In the vicinity of this energy we find LA modes around X with predominant Sn-character. These are, however, slightly too low to account for the cusp in the VDOS. The flattening of LA modes indicates, however, interactions with further optical modes, in particular the Mn-dominated bands which are triply degenerate at Γ at 23 meV. Two of the branches decrease in energy along Γ-X maintaining a considerable Sn-contribution. Supposed that away from the high-symmetry lines the gap between these modes and the LA mode becomes smaller, this can give rise to the above mentioned Sn-feature which nicely coincides with a corresponding feature in the Mn-resolved VDOS. As these Mn-modes should be close to or even lower than the Ni-T$_{2g}$ mode around Γ, the presence of this peak at 17 meV in experiment in combination with the overall excellent agreement of the lower part of the spectrum might be counted as the first, tentative experimental confirmation for the mode inversion in Ni-Mn-based Heusler compounds.

Regarding the high energy part, the agreement between theory and experiment is less obvious. Experiment shows three peaks of similar height, a double peak at 23 and 25 meV and another feature at 29 meV, which corresponds in DFT to two rather small features at 22.3 and 24.2 meV in combination with a paramount double peak at 26.5 and 27.2 meV, which comprises most of the states in the high energy part of the spectrum and results from the collective motion of all three types of

atoms. This discrepancy is not caused by the particular choice of PAW potentials or the semi-local exchange correlation functional. However, it may be affected by subtle changes to the electronic structure of the surrounding metal atoms which interact with Sn (see the discussion in the Appendix). In this sense, also a considerable amount of residual disorder and defects (such as antiphase boundaries) in the experimental sample, which may lead to a spatial inhomogeneity of the individual magnetic moments and projected electronic density of states, can cause a redistribution of the Sn-VDOS. This conjecture will be discussed in the following subsections.

C. Distribution of magnetic moments from Mössbauer measurements and DFT

In order to obtain additional insights into the local magnetism, we employed ^{119}Sn Mössbauer spectroscopy. With this technique, we probe slight deviations in the nuclear energy levels of ^{119}Sn due to the presence of hyperfine interactions. These hyperfine interactions reveal, e.g. the Sn valence state via the isomer shift δ_{iso}. The presence of magnetic ordering leads to the formation of the hyperfine field $B_{\text{hf}}^{\text{Sn}}$ and removes the degeneracy of hyperfine levels. Therefore, a sextet structure occurs in the corresponding spectrum. Due to the filled d-shell, the ^{119}Sn-hyperfine field $B_{\text{hf}}^{\text{Sn}}$ originates from the local environment and is also called the transferred hyperfine field (induced moment).

Figure 4(a) depicts illustrative Mössbauer spectra for Ni$_2$MnSn powder at low, room, and elevated temperatures. Both spectra possess a well-defined spectral fine structure that can be described by a distribution of hyperfine fields $p\left(B_{\text{hf}}^{\text{Sn}}\right)$ (see Fig. 4(b)). For the spectra description, we have used a Hesse Rübartsch distribution[79] describing potential hyperfine field contributions arising from 0 T to 15 T with a stepsize ΔB_{hf} of 0.2 T. To avoid a correlation between linewidth Γ and the standard deviation σ of the hyperfine field distribution $p\left(B_{\text{hf}}^{\text{Sn}}\right)$, we assumed a fixed linewidth $\Gamma = 0.7$ mm/s (natural linewidth of ^{119}Sn is 0.64 mm/s). Since the measured sample is a powder, we assumed the absence of a magnetic texture leading to an intensity ratio of 3:$A_{2,3}$:1:1:$A_{2,3}$:3 for individual sextet subspectra with the intensity ratio of lines 2 and 3, $A_{2,3}$, corresponding to 2. Due to the broad distribution that is present in the studied sample, it is not possible to further investigate the presence of a magnetic texture, due to a correlation of $A_{2,3}$ and $p\left(B_{\text{hf}}^{\text{Sn}}\right)$. In addition, we assumed a linear dependence between the isomer shift of the individual subspectra and the hyperfine field $B_{\text{hf}}^{\text{Sn}}$. Due to the cubic symmetry (also evident in the XRD results (see Ref [40]), we assume a cubic crystal structure and therefore, the absence of a quadrupole splitting ΔE_Q or quadrupole line shift 2ϵ for individual sub spectra in the hyperfine field distribution $p\left(B_{\text{hf}}^{\text{Sn}}\right)$.

The hyperfine field distributions $p\left(B_{\text{hf}}^{\text{Sn}}\right)$ at $T = 4$ K indicate the presence of multiple well-defined contribu-

tions localised at $B_{\text{hf}}^{\text{Sn}} = 9.6$, 6 and 3.8 T. At room temperature, the major contribution occurs at $B_{\text{hf}}^{\text{Sn}} = 5$ T. The other previously mentioned contributions at lower fields could not be well separated in the experiment due to the proximity to the Curie temperature T_{C} that leads to a broad distribution ranging from 0 to 4 T. At these temperatures, the average isomer shift $\langle\delta_{\text{iso}}\rangle$ is 1.50 mm/s and 1.48 mm/s at 4 K and 300 K, respectively. This isomer shifts is in a comparable range with other metallic systems[80] reported in the literature. Looking at the spectra obtained at $T = 360$ K, the Mössbauer spectra reveal a single absorption line centred at 1.44 mm/s. For this temperature, similar description of the experimental data can be derived by assuming a singlet line ($\Gamma = 0.7$ mm/s) or a quadrupole splitting ΔE_Q up to 0.15 mm/s. Nevertheless, structural disorder that may lead to the occur-
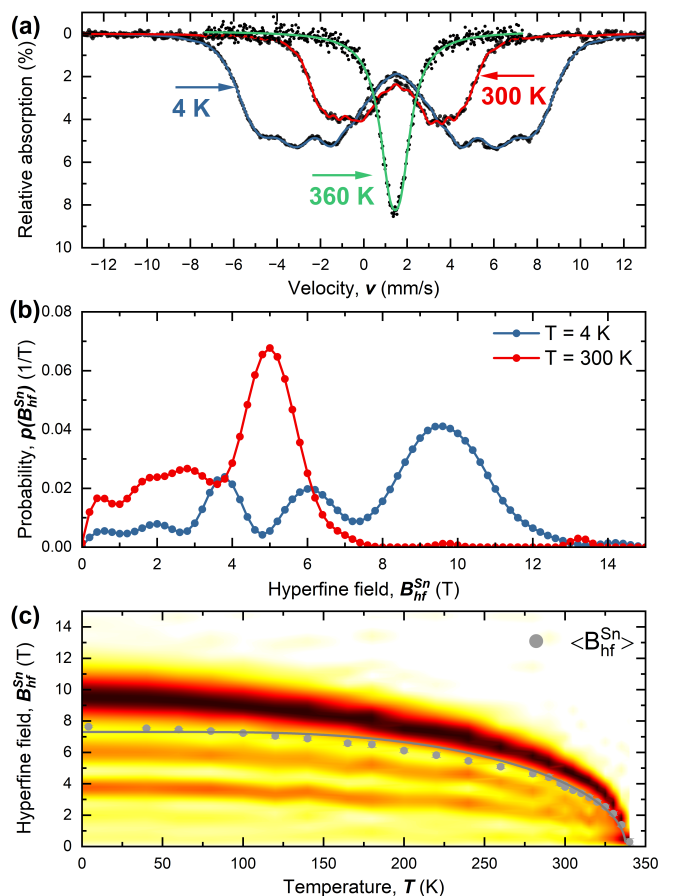

FIG. 4: (a) High temperature ($T = 360$ K, green line), room temperature ($T = 300$ K, red line), and low temperature ($T = 4$ K, blue line) ^{119}Sn-Mössbauer measurements performed in transmission geometry in the absence of a magnetic field and (b) the obtained hyperfine field distribution $p\left(B_{\text{hf}}^{Sn}\right)$ of the respective measurement in the ferromagnetic phase based on a least-squares fit. (c) Temperature dependence of the hyperfine field distribution $p\left(B_{\text{hf}}^{Sn}\right)$ illustrated with a contour plot. The grey dots mark the mean hyperfine field $\langle B_{\text{hf}}^{Sn}\rangle$, while the grey line represents a Brillouin function with a Curie temperature $T_{\text{C}} = 340 \pm 4$ K.

rence of a quadrupole splitting is not sufficiently large to experimentally resolve the splitting the Mössbauer spectrum. Instead, this quadrupole splitting may only lead to a broadening of the resonance. Similar experimental spectra as in Fig. 4(b) were reported in the literature but have not been attributed to anti-site disorder in the respective works[6,8,81]. The absence of significant sextet contributions excludes the formation of large Sn-containing secondary phases that possess higher ordering temperatures.

In a system with perfect L2$_1$ ordering, we would assume that Sn only occupies the $4a$ position with the Ni atoms as the nearest neighbours (NN) occupying the $8c$ positions and the Mn atoms at the $4b$ sites with an Sn-Mn bond length of approximately 3 Å. This local environment would lead to the presence of a single hyperfine contribution. Instead, we observe the presence of three distinct hyperfine field contributions at low temperatures. Assuming multiple Gaussian distributions, the deconvolution of the obtained hyperfine field distribution $p\left(B_{\mathrm{hf}}^{\mathrm{Sn}}\right)$ at $T = 4\,\mathrm{K}$ indicates that approximately 70 % of the hyperfine field contributions are located at $B_{\mathrm{hf}} = 9.6\,\mathrm{T}$ with a full width at half maximum (FWHM) of 2.77 T, while the remaining major contributions at 6 T and 3.8 T contribute with 16 % and 14 % exhibiting the FWHM of 1.49 T and 1.1 T, respectively. This leads to the assumption that only 70 % of the spectral area possess an environment corresponding to perfect L2$_1$-ordering. The remaining 30 % of the spectral area might possess different local environments originating from the deviation of the pure 2-1-1 stoichiometry depicted from our ICP-OES measurements.

Figure 4(c) illustrates the thermal evolution of the hyperfine field distribution $p\left(B_{\mathrm{hf}}^{\mathrm{Sn}}, T\right)$ as a contour plot. This shows that the different magnetic contributions of Sn are present in the whole temperature range up to T_{C}, and all contributions exhibit similar thermal responses. In a first-order approximation, the mean hyperfine field $\left\langle B_{\mathrm{hf}}^{Sn}\right\rangle$ can be described by a Brillouin function with a $T_{\mathrm{C}} = 340\pm4\,\mathrm{K}$ and $J = 0.5$. Looking at the thermal evolution of the hyperfine field, it is evident that the system possesses a second-order phase transition, while no co-existence of the FM and paramagnetic phase is present. Within the contour plot a lightly-shaded yellow area is present e.g. above $B_{\mathrm{hf}}=8\,\mathrm{T}$ at $T = 300\,\mathrm{K}$. These contributions can be considered as noise originating from the experimental spectra (see for comparison Fig. 4(b)) and indicates an estimate for an error bar.

The experimental evidence for several non-equivalent Sn sites with different magnetic properties calls for a corresponding analysis of the site-resolved partial and total magnetic moments in partially disordered cells, which is summarized in Table I. These results are consistent with detailed theoretical investigation in Ref. 26, only slight differences arising from different computational setup are encountered. The 16-atoms supercell contains eight Ni, four Sn and four Mn atoms. In the defect-free L2$_1$-phase Ni$_2$MnSn, all Sn atoms located at the $(4a)$ Sn sublattice

exhibit the same magnetic moment of -0.052 μ_{B}/atom, see Table I. The negative sign indicates that the magnetic moment has an antiparallel orientation to the total magnetic moment of the whole supercell. Similarly, Mn atoms also exhibit equivalent local magnetic moment of 3.585 μ_{B}/atom.

When we introduce an anti-site disorder, the symmetry is reduced, i.e., the neighbourhood of atoms of the same type becomes different and thus some atoms are no longer symmetry-equivalent. In the case of the Mn$\leftrightarrow$Ni swapping, the swapped Mn atom at the $8c$ site, Mn$_{8c}$, has a smaller magnetic moment than Mn$_{4b}$. The swapped Mn$_{8c}$ atoms affect the NN Sn atoms (at the distance of about 2.6 Å), which increases their magnetic moment. As a consequence, there are two magnetic types of Sn for Mn$\leftrightarrow$Ni anti-site disorder in 16-atom supercell. One exhibits the magnetic moment of -0.061 μ_{B} and these Sn atoms have one NN Mn atom and four Mn atoms as the next nearest neighbors (NNN). The second type of Sn atoms possesses a local magnetic moment of -0.071 μ_{B} and these Sn atoms have one Mn as NN and six as NNN.

If we consider anti-site disorder arising from swapping between Mn and Sn, this even results in three different types of Sn. A swapped Sn$_{4b}$ atom, that went to the Mn sublattice and has only two NNN Mn, has a tiny moment of -0.013 μ_{B}. The magnetic moments of the other Sn$_{4a}$ atoms with -0.052 and -0.059 μ_{B} are close to the value in the ideal L2$_1$ structure. The three magnetic types of Sn atoms discussed above correlate with the the three maxima in the experimental hyperfine field distributions at 4 K (at 3.8, 6, and 9 T in blue curve of Fig. 4), which might be considered as an argument for presence of Mn$\leftrightarrow$Sn anti-site disorder in the experimental sample.

Another important cause for a symmetry reduction originates from magnetism. Here, the atoms do not change sites, but if one Mn atom re-orients its local magnetic moment to the direction antiparallel to the direction of the total magnetic moment, the electronic environment changes for the neighboring atoms as well. Reorienting one Mn spin in the L2$_1$ case results in a FiM structure with two types of induced Sn moments. Both are smaller in magnitude in comparison to the FM case, see Table I.

Both sources of reduced symmetry are combined when the Mn atom swaps with either Ni or Sn atom and the swapped Mn atom (at either the Ni or Sn sublattice, correspondingly) reverses the orientation of its magnetic moment. Disordered Mn$\leftrightarrow$Ni and Mn$\leftrightarrow$Sn structures again have two and three magnetic types of Sn atoms, respectively. For the system with swapped Mn and Ni atoms, Sn atoms are strongly affected by the NN Mn$_{8c}$ atoms with the magnetic moment oriented antiparallel to magnetic moments of Mn$_{4b}$ atoms. In the case of Mn$\leftrightarrow$Sn disorder, the impact of the Mn$_{4a}$ atom at the Sn sublattice, that has the orientation of its local magnetic moment antiparallel to that of the Mn$_{4b}$ atoms at the Mn sublattice, is weaker on Sn$_{4a}$ atoms because of quite large distances between them (about 4.3 Å between Mn$_{4b}$ and Sn$_{4a}$). Meantime, the magnetic moment of swapped Sn$_{4b}$ (Sn$_4$

TABLE I: Site-resolved local magnetic moments of atoms (μ_i) and the total magnetic moments (μ_{tot}) of Ni_2MnSn in $L2_1$ structure and structures with anti-site disorder with FM and FiM ordering. In the 16-atom supercell, we find four Sn and four Mn atoms, denoted by the indices. In the ideal $L2_1$ case, the surrounding of all Sn_i atoms are equivalent, and they show the same corresponding magnetic moments. When the symmetry is reduced due to either magnetic or anti-site disorder, Sn_i magnetic moments induced by Mn moments become inequivalent for different sites i. For Ni, averaged absolute values are presented, as individual moments are similar; only for Mn↔Ni swapping (marked by asterisk) we encounter a significant variation across the sites.

| | | μ_i [μ_B/atom] | | | | | | | | | μ_{tot} |
		Sn_1	$|Sn_2|$	Sn_3	Sn_4	Mn_1	$|Mn_2|$	$Mn_3|$	Mn_4	Ni	[μ_B/f.u.]
$L2_1$	FM	-0.052				3.585				0.241	4.090
	FiM	-0.015		-0.010		3.628			-3.589	0.182	2.235
Mn↔Ni	FM	-0.071		-0.061		3.462			3.039	0.186*	3.724
	FiM	-0.014		-0.026		3.480			-3.119	0.147*	2.055
Mn↔Sn	FM	-0.052		-0.059	-0.013	3.603	3.734	3.529		0.272	4.164
	FiM	-0.050		-0.041	0.034	-3.678	3.653	3.543		0.102	1.969

in the last line of Table I) aligns antiparallel to the Sn_{4a} moments since it has two Mn_{4b} atoms as NNN.

D. Impact of site-disorder on the VDOS

As the DFT calculations show that magnetic and anti-site disorder may explain the trends observed in ^{119}Sn-Mössbauer spectroscopy, we evaluate the VDOS for these systems in order to improve the agreement between the high-energy part of the experimental and theoretical Sn-VDOS. The total and element-resolved VDOS for all structures are presented in Fig. 5. Note, that Ni contribution is taken per two atoms as presented in the Ni_2MnSn unit cell. As discussed in Sec. III B, the VDOS for ordered $L2_1$ structure (Fig 5(a)) already provides a reasonable agreement with experiment at energies below 23 meV. However, the paramount high energy peak at ≈ 27 meV, which arises from the hybridization of Ni, Mn, and Sn modes and is thus present in all partial contributions, appears in the experimental spectrum in Fig. 2, but with a significantly smaller height.

At this point, one should note that changing the treatment of exchange and correlation by applying an additional Hubbard-U term to the Mn-d states in the FM $L2_1$ structure may also effectively remove weight from the huge peak in the Sn-VDOS at 27 meV in favor of the smaller feature at 23 meV. However, within this description a pronounced gap-like feature opens in between the peaks at the same time, which is not seen in the experimental Sn-VDOS (a detailed discussion is given in the Appendix). To unveil the potential origin of the remaining discrepancies between experiment and calculations, we therefore continue to analyze the impact of different types of disorder on vibrational properties in the framework of the GGA, keeping in mind that methodological changes in the treatment of electronic correlations on the transition metal sites may involve secondary corrections to the Sn-VDOS as well.

Considering first the magnetic disorder in $L2_1$ system, it is known that a complex magnetic behaviour may occur

in Ni-Mn-based ternaries due to the competition between the antiferromagnetic and FM interactions associated with magnetic sublattices containing Mn atoms[9,17,82,83]. Therefore, we have computed VDOS also for a FiM configuration of $L2_1$-Ni_2MnSn, see Fig. 5(d).

Changing the direction of one Mn magnetic moment results in changing some features in partial and total VDOS. In particular, one can see the splitting in both Sn and Ni VDOS at 5 and 7 meV and rearrangement of Ni-VDOS at 16–19 meV, where the mode inversion takes place. Also, due to the hybridization of Mn and Ni modes at 25 meV, one can see the splitting in Ni-VDOS and – as a result – total VDOS at 25 and 26 meV. However, magnetic disorder does not bring too much qualitative changes in the total and partial Sn VDOS, and the high peak at $25 - 26$ meV is still there.

Following the conjecture that chemical disorder is one likely origin of the remaining disagreement between experimental and calculated VDOS in the high-energy region, we examined the sensitivity of VDOS to anti-site defects, in particular swapped pairs of Mn↔Ni and Mn↔Sn atoms. Our choice was motivated by our recent study of these defects in the stoichiometric Ni_2MnSn[26]. When introducing one pair of swapped atoms per 16-atom supercell, these stoichiometry-preserving defects increase the energy by only moderate amounts, in particular, the Mn↔Ni swap by 0.055 eV/atom and the Mn↔Sn one by 0.075 eV/atom. These values were obtained when the local magnetic moment of the Mn atom at the Ni/Sn sublattice has the orientation parallel to those of Mn atoms at the Mn sublattice, i.e. for the FM state.

We also examined the FiM state when the orientation of the swapped Mn atom at the Ni/Sn sublattice is antiparallel to the local magnetic moments of Mn atoms at the Mn sublattice. The energy increases were then slightly different, $\Delta E = 0.054$ eV/atom in the case of the Mn-Ni swap and $\Delta E = 0.075$ eV/atom in the case of the Mn-Sn swap. Importantly, these defects significantly reduce the symmetry and result in many different local environments of Sn atoms. The studied types of disorder, i.e. the anti-site, magnetic or combined, have thus a mas-
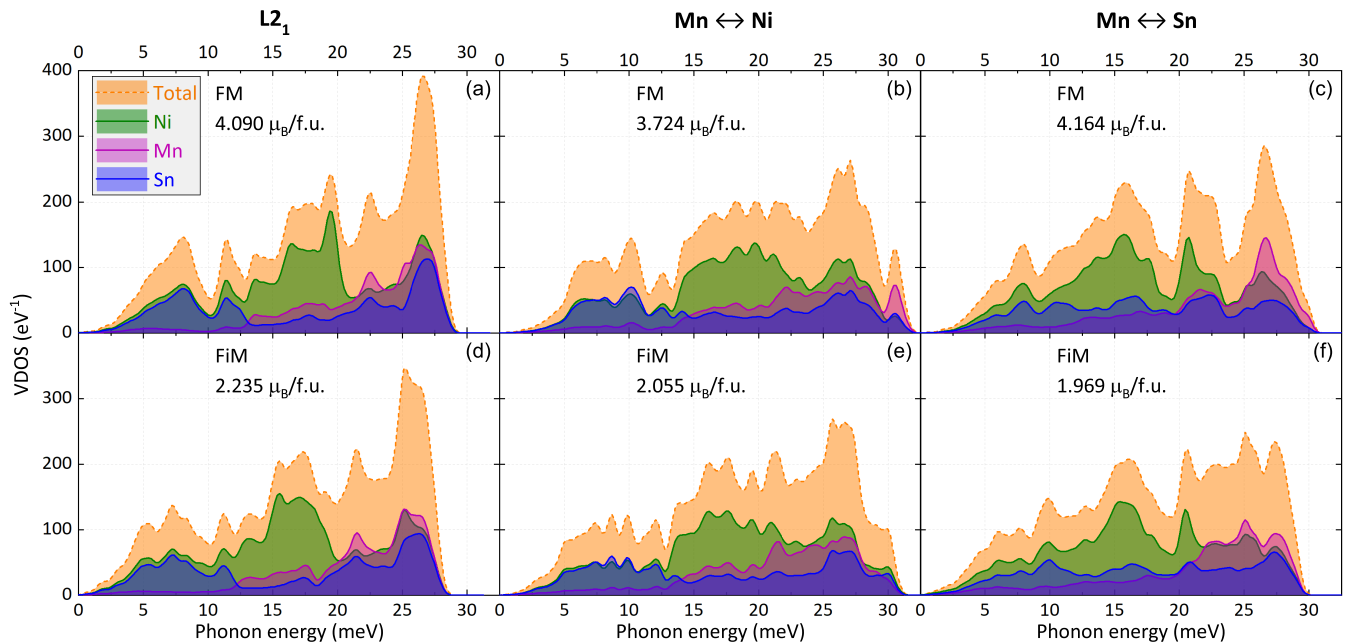
FIG. 5: Calculated total and element-resolved VDOS for the ideal L2$_1$ structure (a,d) and systems with anti-site disorder introduced by swapping of Mn and Ni atoms (b,e) and Mn and Sn atoms (c,f). Smearing width of 0.0725 THz is used for better visibility. Results for the FM and FiM configurations are presented in parts (a-c) and (d-f), respectively. The magnetic moments of each structure (in μ_B/f.u.) are given in the figures.

sive impact on the Sn atoms including their vibrational properties. These results are summarized in Fig. 5(d-f).

Figures 5(b,e) show the VDOS for FM and FiM configurations with Mn↔Ni anti-site disorder. One can note a significant redistribution of the VDOS in the whole energy range. The entire VDOS weight is shifted by 2.5 meV to higher energy in comparison with the L2$_1$ structure. Taking into account this shift, we can notice that the two first peaks at 8 and 11 meV in Fig. 5(a) redistribute with disorder and split into three: one broad at $6 - 8$ meV and two sharp ones at 10 and 12.5 meV, which, nevertheless, still show signs of Ni-Sn hybridization. In the middle-range, the distribution of Ni atoms vibrating with energies from 13 to 24 meV becomes more homogeneous. Besides, the contribution from Sn atoms increases at $13.5 - 19$ meV and significantly decreases at ≈ 27 meV yielding a better agreement with the experiment. Introducing magnetic disorder in this system (Fig. 5(e)) also results in a splitting of the VDOS peaks at low energies ($5 - 15$ meV) in comparison with FiM L2$_1$ (Fig. 5(d)) as well as in the decrease in the Mn-VDOS around 30.5 meV, which is clearly visible for FM case in Fig. 5(b).

Significant changes in total and partial VDOS are also found for the system with swapped Mn and Sn atoms, see Fig. 5(c). There are four peaks in the total VDOS formed by the hybridization of Ni and Sn modes (at 7.9 and 15.7 meV) and of Ni, Mn, and Sn (at 21 and 27 meV). In contrast to L2$_1$, the highest peak at 27 meV in the total VDOS is formed mostly by hybridization of

Mn and Ni modes. Meantime, Sn contribution to the high-frequency vibrations becomes much smaller in comparison with other constituents, and Sn-VDOS distribution appears to be more homogeneous in the whole energy range. FiM alignment changes the situation at high frequencies and affects the vibrations of all atoms, see Fig. 5(f). In particular, one can notice a splitting in the Mn VDOS in the range of $21 - 27$ meV, whereas in the Sn-VDOS the 27 meV peak becomes again sharper. Thus, anti-site disorder introduced by swapping between pairs Mn↔Ni and Mn↔Sn changes the hybridization modes and strongly affects low-, middle-, and high-frequency ranges of VDOS profiles.

To summarize the discussion, we compare in Fig. 6 the Sn-partial VDOS calculated for all ordered and disordered systems (summary of blue curves from Fig. 5), both for FM (solid lines) and FiM (dashed lines) configurations with the experimental data. From the experimental Sn-VDOS, the largest Sn contribution is seen for low-frequency vibrations, while DFT VDOS of Sn in the ideal L2$_1$ structure differs qualitatively in this respect and shows a high peak in the high energy range. In turn, the overall shape of the low energy part is reproduced very well, but it also appears to be somewhat sharper from theory.

Introducing the disorder changes the Sn-VDOS spectrum and diminishes the high-frequency part. The prominent features at 8 and 11 meV are still visible in most cases, but appear to be smeared out considerably. The FM alignment provides a better agreement
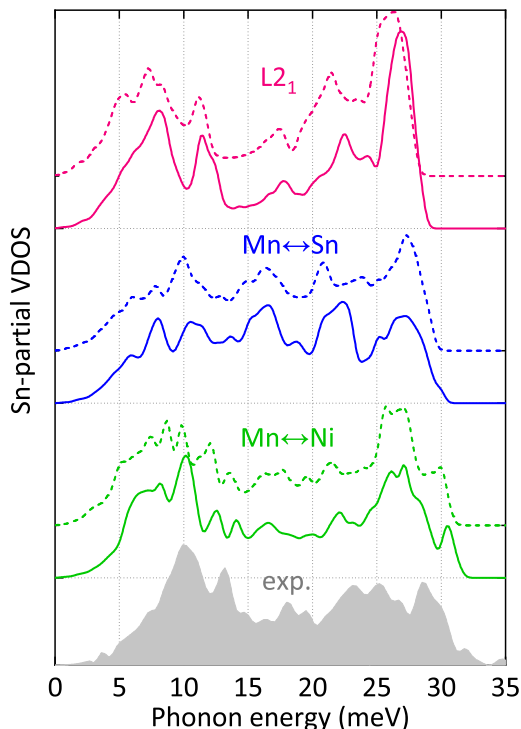
FIG. 6: Calculated Sn-VDOS for the ideal L2$_1$ and disordered structures of Ni$_2$MnSn in comparison with the results of NRIXS measurements (grey). Results of DFT calculations are presented for FM (solid lines) and FiM (dashed lines) ordering.

with the experiment compared to the FiM arrangement, which goes hand in hand with an enhancement of the Sn-VDOS features at high frequencies. In conclusion, we do not obtain a perfect fit between the experiment and neither case of site-disorder, only partial improvements for different parts of the spectra. However, we may expect that a real sample may be subject to a complex superposition of different structural and magnetic defects.

IV. CONCLUSIONS

By combining DFT calculations with NRIXS and Mössbauer spectroscopy involving [119]Sn nuclear resonance, we were able to disentangle the vibrational and magnetic contributions of the main group element in a near-stoichiometric Ni$_2$MnSn Heusler compound. DFT calculations are able to reproduce the Sn-selective VDOS obtained by NRIXS particularly well in the low energy region, whereas the highest modes are underestimated by 2-3 meV in the GGA-DFT calculations. Based on a detailed comparison of the VDOS obtained by LDA, GGA and GGA+U and PAW potentials with and without d-semicore electrons, see the Appendix, we relate this shortcoming to the well-known underbinding of the 4th-row elements within the GGA, which is more significant as compared to the third row transition metals.

In turn, in the low energy part, the GGA provides a very good agreement with experiment, which is much better than from LDA. This allows us to relate the features in the experimental VDOS to features in the element-resolved phonon band structure of perfectly L2$_1$-ordered Ni$_2$MnSn. In this way, we can provide evidence from experiment that the band inversion feature in Ni-Mn-based Heusler alloys[62,63], which shows up as a large, dominating Ni contribution in the energy range between 13 and 20 meV, is also present in Ni$_2$MnSn and may thus contribute to the softening of transversal acoustic modes along Γ-K and potentially also at X. The high energy part of the Sn-VDOS differs from experiment, apart from the too low cut-off, by a paramount peak resulting from strongly hybridized modes of all elements, which is not encountered in experiment, and may thus indicate a deviation from perfect L2$_1$ order.

Mössbauer spectroscopy at low temperatures reveals the presence of several inequivalent Sn-sites, which indicates the presence of a considerable amount of site-disorder and other defects (such as e. g. antiphase boundaries) in the sample. The comparison of the site-resolved VDOS obtained with different kinds of site-disorder realized in a 16-atom cell shows that the large features at high energies are indeed susceptible to changes in the electronic structure of the environment. These may arise e. g. from chemical or magnetic disorder or particular modelling of exchange and correlation on the transition metal sites, which explains the remaining differences between the experimental and calculated Sn-VDOS.

Since the NRIXS measurements have been performed at cryogenic temperatures we can consider the harmonic approximation sufficient for the comparison of the VDOS. Nevertheless, it may be interesting to investigate in future finite temperature modification of the phonon spectrum. In the simplest approach this can be achieved in terms of the quasiharmonic approximation including magnetic excitations, which is already capable to capture the thermodynamics of the martensitic transitions in Ni$_2$MnGa accurately[71,84]. A finite temperature renormalization of the dispersion and VDOS arising from phonon-phonon interactions may be expected at ambient conditions and beyond and might partly account for the differences between the experimental spectra obtained at 15 K and 300 K. This can be modelled using for instance the Self-Consistent Ab-Initio Lattice Dynamics[85,86] (SCAILD) or the Temperature Dependent Effective Potential method[87] (TDEP). These schemes are, however, computationally very demanding and beyond the scope of the present work.

Our findings show that in combination with DFT isotope selective Mössbauer spectroscopy and NRIXS the main-group element, Sn, can be used effectively as a powerful probe to characterize details of vibrational, magnetic and symmetry-related properties of a transition metal compound. Particular deviations between theory and experiment can be discussed in terms of structural and magnetic defects. In turn, the good agreement

with experimental data documents the predictive power of DFT within the GGA also for the vibrational properties of Heusler compounds with main group elements from the 4th row.

V. ATTRIBUTIONS

VI. ACKNOWLEDGMENTS

Appendix

A. Tests of potentials

One of the most interesting features of our theoretical Sn-VDOS in Ni_2MnSn, see Fig. 5, is the peak at about 27 meV close to the top-most frequencies that is much less pronounced in the experimental data. While we have addressed this discrepancy between the theory and experiments above by discussing the influence of chemical disorder (anti-sites defects) and magnetic disorder, our
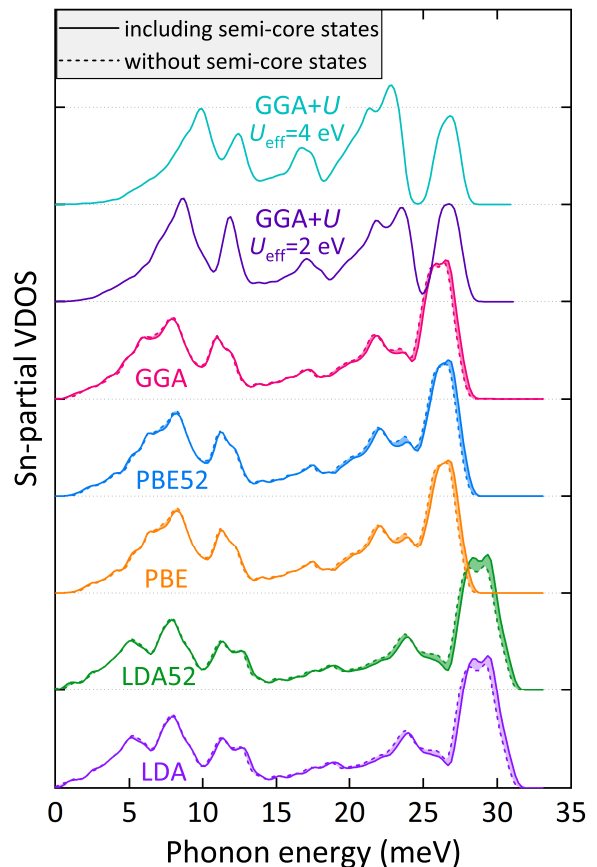

FIG. 7: Calculated Sn-VDOS for the ideal $L2_1$-Ni_2MnSn using different GGA and LDA potentials. Results of DFT calculations are presented for potentials that include semi-core electron states (solid lines) as well as those without them (dotted lines).

computational set-up should also be checked. In particular, our quantum-mechanical calculations were performed not for all electrons of the constituting atoms but only a smaller set of valence electrons. As our results slightly depend on the choice of the used (pseudo-)potentials provided by the developers of the VASP code, we next use other available potentials and compare the results.

Our theoretical results summarized above were all obtained when using one of the most recent sets of potential files, so-called PBE.52 collection, and we have chosen potentials with an extended set of semi-core electronic states, in particular the files named as Ni_pv, Mn_pv and Sn_d. Therefore, we next compare our results with those obtained when using the potentials from (i) the LDA and LDA.52 (Perdew-Zunger parametrization of Ceperley-Alder (CA) Monte-Carlo correlation data, Refs. 88,89) collection of potentials, (ii) PBE and PBE.52 (Perdew-Burke-Ernzerhof parametrization, Ref. 59) collections and (iii) GGA (Perdew-Wang, PW91, Ref. 90) collections of potentials. For all the above mentioned types of potentials, we tested also those with

and without additional p and d semi-core states, e.g. the Mn_pv and Mn files, respectively. The calculations were performed for fully relaxed L2$_1$-structure Ni$_2$MnSn. The atomic displacements were calculated using 108-atom supercells obtained as $3 \times 3 \times 3$ multiples of the 4-atom primitive cell of L2$_1$-structure Ni$_2$MnSn.

The comparison in Fig. 7 allows for drawing a few important conclusions. First, that the very pronounced peak close to the top-most frequencies is present in Sn-VDOS in the perfect L2$_1$-Ni$_2$MnSn for all other sets of potentials that we tested with LDA and GGA exchange-correlation functionals. Second, all potentials distributed for different parametrizations of the generalized gradient approximation, i.e. the collections named GGA, PBE and PBE.52, predict the highest phonon frequency close to 27 meV. This finding is true for both, potentials that contain the semi-core states, i.e. the potential files named Ni_pv, Mn_pv and Sn_d, as well as those without these electron states, i.e. the potential files named Ni, Mn and Sn. Lastly, the LDA and LDA.52 potentials with the semi-core states, as well as without them, have the Sn-VDOS covering a wider range up to higher frequencies of about 32 meV. This wider range of frequencies is in a better agreement with the range of our experimental data. The LDA potentials are, nevertheless, not suitable for the studied system as all the four LDA-related calculations predict the perfect L2$_1$-Ni$_2$MnSn to be unstable. In particular, the LDA calculations result in a number of imaginary-frequency phonon modes (not shown in Fig. 7). These frequencies would imply that the perfect L2$_1$-Ni$_2$MnSn is unstable as a major disagreement with experimental data.

It is also worth mentioning that previous phonon calculations of the defect-free Ni$_2$MnSn resulted in very similar VDOS. For example, the total VDOS in Ref. 30 exhibits quite a similar peak close to the highest frequencies. The authors of Ref. 30 did not publish the Sn-resolved VDOS but our calculations show that the peak in the total VDOS at the highest frequencies combines contributions from vibrations of all three chemical species. Therefore, we expect a pronounced peak close to the highest phonon frequencies in the computed partial Sn-VDOS, too.

B. Calculations with Hubbard-U correction

In addition, we analyzed the impact of a semi-empirical Hubbard-U correction applied to the Mn-sites on the Sn-VDOS. Here, we employed the rotationally invariant scheme of Dudarev *et al.*[49], where the correction can be expressed in terms of an effective $U_{\text{eff}} = U - J$, parameter with U corresponding to the effective on-site Coulomb interaction and J to the exchange. We employed moderate corrections $U_{\text{eff}} = 2\,\text{eV}$ and $4\,\text{eV}$, which are consistent with values used in previous studies on Ni$_2$MnSn, Ni$_2$MnGa and α-Mn[52–54]. We used the PBE semicore potentials Ni_pv, Mn_pv, and Sn_d as described above, with consistent numerical settings in a $4 \times 4 \times 4$ extension of the primitive cell for calculating the VDOS. The on-site Coulomb correction typically leads to an enhanced localization of the Mn states, which expresses here in terms of an increased magnetic moment on the Mn sites in combination with an increased lattice parameter, which both tend to exceed the experimental values considerably in contrast to the plain GGA (see the SM[40] for all data and a more detailed discussion). Most interesting, the electronic changes on the Mn-sites show a remarkable impact on the partial VDOS of Sn, which was not subject to this correction and treated with plain PBE as shown by the topmost two spectra in Fig. 7: Applying $U_{\text{eff}} = 2\,\text{eV}$ decreases the peak at 27 meV and redistributes high-energy Sn-VDOS weight to the lower range between 18 and 25 meV. This renders the most prominent peaks similar in height, similar to the swapping of Mn and Sn atoms, which comes closer to the experimental VDOS as shown in Fig. 6. However, with PBE+U a marked pseudogap opens at 25 meV, which separates the high-energy modes from the middle range. This is neither seen in the experiment nor in any of the GGA calculations with partial disorder. Increasing U_{eff} to 4 eV reverses the height of the peaks at 23 and 27 meV and further deepens the spurious gap, revealing a marked dependence of the Sn-VDOS on the localization of the d-electrons at the Mn sites, which is controlled by the parameter U_{eff}. Thus, while not necessarily providing an improvement to the modeling of magnetic and vibrational properties of Ni$_2$MnSn in general, the application of an additional Hubbard-U term demonstrates clearly the sensitivity of the Sn VDOS and thus its interatomic force constants to delicate changes in the electronic and magnetic properties at the surrounding metal sites.

* corresponding author: olga.miroshkina@uni-due.de

[1] T. Graf, C. Felser, and S. S. Parkin, Prog. Solid. State Ch. **39**, 1 (2011).

[2] P. J. Webster, Contemp. Phys. **10**, 559 (1969).

[3] J. Kaštil, J. Kamarád, O. Isnard, Y. Skourski, M. Míšek, and Z. Arnold, J. Alloys Compd. **650**, 248 (2015).

[4] A. L. Alves, A. Magnus Gomes Carvalho, J. R. Cápua Proveti, V. P. Nascimento, and E. C. Passamani, Mater. Charact. **158**, 109972 (2019).

[5] R. N. Kuzmin, N. S. Ibraimov, and G. S. Zhdano, Sov. Phys. JETP **23**, 219 (1966).

[6] W. Leiper, D. J. W. Geldart, and P. J. Pothier, Phys. Rev.

B **3**, 1637 (1971).

[7] Williams, J. M. and Danson, D. P., Le Journal de Physique Colloques **40**, C2 (1979).

[8] A. G. Gavriliuk, G. N. Stepanov, V. A. Sidorov, and S. M. Irkaev, J. Appl. Phys. **79**, 2609 (1996).

[9] P. J. Brown, J. Crangle, T. Kanomata, M. Matsumoto, K.-U. Neumann, B. Ouladdiaf, and K. R. A. Ziebeck, J. Phys. Condens. Matter **14**, 10159 (2002).

[10] E. Yüzüak, I. Dincer, Y. Elerman, A. Auge, N. Teichert, and A. Hütten, Appl. Phys. Lett. **103**, 222403 (2013).

[11] O. Gutfleisch, T. Gottschall, M. Fries, D. Benke, I. Radulov, K. P. Skokov, H. Wende, M. Gruner, M. Acet, P. Entel, et al., Philosophical Transactions of the Royal Society A: Mathematical, Phys. Eng. Sci. **374**, 20150308 (2016).

[12] E. Sasioglu, L. M. Sandratskii, and P. Bruno, Phys. Rev. B **71**, 214412 (2005).

[13] S. K. Bose, J. Kudrnovský, V. Drchal, and I. Turek, Phys. Rev. B **82**, 174402 (2010).

[14] S. K. Bose, J. Kudrnovský, V. Drchal, and I. Turek, Phys. Rev. B **84**, 174422 (2011).

[15] T. Fichtner, G. Kreiner, S. Chadov, G. H. Fecher, W. Schnelle, A. Hoser, and C. Felser, Intermetallics **57**, 101 (2015).

[16] D. Comtesse, M. E. Gruner, M. Ogura, V. V. Sokolovskiy, V. D. Buchelnikov, A. Grünebohm, R. Arróyave, N. Singh, T. Gottschall, O. Gutfleisch, et al., Phys. Rev. B **89**, 184403 (2014).

[17] P. Entel, M. Siewert, M. E. Gruner, H. C. Herper, D. Comtesse, R. Arróyave, N. Singh, A. Talapatra, V. V. Sokolovskiy, V. D. Buchelnikov, et al., Eur. Phys. J. B **86**, Art. No. 65 (2013).

[18] A. Planes, L. Mañosa, and M. Acet, J. Phys. Condens. Matter **21**, 233201 (2009).

[19] L. Mañosa, X. Moya, A. Planes, S. Aksoy, M. Acet, E. F. Wassermann, and T. Krenke, Mater. Sci. Forum **583**, 111 (2008).

[20] E. Stern-Taulats, A. Planes, P. Lloveras, M. Barrio, J.-L. Tamarit, S. Pramanick, S. Majumdar, S. Yüce, B. Emre, C. Frontera, et al., Acta Mater. **96**, 324 (2015).

[21] S. Singh, L. Caron, S. W. D'Souza, T. Fichtner, G. Porcari, S. Fabbrici, C. Shekhar, S. Chadov, M. Solzi, and C. Felser, Adv. Mater. **28**, 3321 (2016).

[22] F. Scheibel, T. Gottschall, A. Taubel, M. Fries, K. P. Skokov, A. Terwey, W. Keune, K. Ollefs, H. Wende, M. Farle, et al., Energy Technol. **6**, 1397 (2018).

[23] A. Waske, B. Dutta, N. Teichert, B. Weise, N. Shayanfar, A. Becker, A. Hütten, and T. Hickel, Energy Technol. **6**, 1429 (2018).

[24] A. Grünebohm, H. C. Herper, and P. Entel, J. Phys. D Appl. Phys. **49**, 395001 (2016).

[25] O. Benguerine, Z. Nabi, B. Benichou, B. Bouabdallah, H. Bouchenafa, M. Maachou, and R. Ahuja, Revista Mexicana de Fisica **66**, 121 (2020).

[26] M. Friák, M. Mazalová, I. Turek, A. Zemanová, J. Kaštil, J. Kamarád, M. Míšek, Z. Arnold, O. Schneeweiss, M. Všianská, et al., Materials **14**, 523 (2021).

[27] J. Kübler, A. R. Williams, and C. B. Sommers, Phys. Rev. B **28**, 1745 (1983).

[28] F. Cugini, S. Chicco, F. Orlandi, G. Allodi, P. Bonfá, V. Vezzoni, O. N. Miroshkina, M. E. Gruner, L. Righi, S. Fabbrici, et al., Phys. Rev. B **105**, 174434 (2022).

[29] B. Dutta, I. Opahle, and T. Hickel, Funct. Mater. Lett. **09**, 1642010 (2016).

[30] S. Ağduk and G. Gökoğlu, J. Alloys Compd. **511**, 9 (2012).

[31] V. Recarte, M. Zbiri, M. Jiménez-Ruiz, V. Sánchez-Alarcos, and J. Pérez-Landazábal, J. Phys. Condens. Matter **28**, 205402 (2016).

[32] M. Friák, M. Mazalová, I. Turek, O. Schneeweiss, J. Kaštil, J. Kamarád, and M. Šob, Mater. Trans. **63**, 430 (2022).

[33] U. von Hörsten, *Pi program package, a windows program for the evaluation of mössbauer spectra. Download at* `http://udue.de/Pi` (2022).

[34] A. H. Said, H. Sinn, T. S. Toellner, E. E. Alp, T. Gog, B. M. Leu, S. Bean, and A. Alatas, J. Synchrotron Radiat. **27**, 827 (2020).

[35] T. S. Toellner, A. Alatas, A. Said, D. Shu, W. Sturhahn, and J. Zhao, J. Synchrotron Radiat. **13**, 211 (2006).

[36] T. S. Toellner, A. Alatas, and A. H. Said, J. Synchrotron Radiat. **18**, 605 (2011).

[37] R. Röhlsberger, *Nuclear Condensed Matter Physics with Synchrotron Radiation* (Springer Berlin Heidelberg, 2005).

[38] Y.-L. Chen and D.-P. Yang, *Mössbauer Effect in Lattice Dynamics: Experimental Techniques and Applications* (Wiley-VCH, 2007).

[39] N. Dauphas, M. Y. Hu, E. M. Baker, J. Hu, F. L. H. Tissot, E. E. Alp, M. Roskosz, J. Zhao, W. Bi, J. Liu, et al., J. Synchrotron Radiat. **25**, 1581 (2018).

[40] See Supplemental Material at http://... for the additional information about the data evaluation of the nuclear inelastic x-ray scattering (NRIXS) spectra, comparison of the polycrystalline bulk Ni_2MnSn ingot and the prepared powder with ^{119}Sn-Mössbauer spectroscopy, and x-ray diffraction measurements as well as the impact of different exchange-correlation functionals (GGA, GGA+U, meta-GGA, and hybrid functionals) on the ground state properties obtained in the framework of DFT.

[41] D. W. Johnson and J. C. H. Spence, J. Phys. D Appl. Phys. **7**, 771 (1974).

[42] K. S. Singwi and A. Sjölander, Phys. Rev. **120**, 1093 (1960).

[43] W. Sturhahn, T. S. Toellner, E. E. Alp, X. Zhang, M. Ando, Y. Yoda, S. Kikuta, M. Seto, C. W. Kimball, and B. Dabrowski, Phys. Rev. Lett. **74**, 3832 (1995).

[44] H. J. Lipkin, Phys. Rev. B **52**, 10073 (1995).

[45] W. Sturhahn, Hyperfine Interact. **125**, 149 (2000).

[46] W. Sturhahn, J. Phys.: Condens. Matter **16**, S497 (2004).

[47] I. Unzueta, J. López-García, V. Sánchez-Alarcos, V. Recarte, J. I. Pérez-Landazábal, J. A. Rodríguez-Velamazán, J. S. Garitaonandia, J. A. García, and F. Plazaola, Appl. Phys. Lett. **110**, 181908 (2017).

[48] J. Rodríguez-Carvajal, Phys. B: Condens. Matter. **192**, 55 (1993), ISSN 0921-4526.

[49] S. L. Dudarev, G. A. Botton, S. Y. Savrasov, C. J. Humphreys, and A. P. Sutton, Phys. Rev. B **57**, 1505 (1998).

[50] J. Sun, A. Ruzsinszky, and J. P. Perdew, Phys. Rev. Lett. **115**, 036402 (2015).

[51] A. V. Krukau, O. A. Vydrov, A. F. Izmaylov, and G. E. Scuseria, J. Chem. Phys. **125**, 224106 (2006).

[52] B. Hamri, B. Abbar, A. Hamri, O. Baraka, A. Hallouche, and A. Zaoui, Comput. Condens. Matter **3**, 14 (2015).

[53] T. Koubský, P. Sedlák, H. Seiner, J. Fojtíková, M. Obata, T. Oda, and L. Kalvoda, Acta Phys. Pol. A **134**, 2019 (2018).

[54] A. Pulkkinen, B. Barbiellini, J. Nokelainen, V. Sokolovskiy,

D. Baigutlin, O. Miroshkina, M. Zagrebin, V. Buchelnikov, C. Lane, R. S. Markiewicz, et al., Phys. Rev. B **101**, 075115 (2020).

[55] V. D. Buchelnikov, V. V. Sokolovskiy, O. N. Miroshkina, M. A. Zagrebin, J. Nokelainen, A. Pulkkinen, B. Barbiellini, and E. Lähderanta, Phys. Rev. B **99**, 014426 (2019).

[56] W. Stieler, M. Hillberg, F. Litterst, C. Böttger, and J. Hesse, Nuclear Instruments and Methods in Physics Research Section B: Beam Interactions with Materials and Atoms **95**, 235 (1995).

[57] G. Kresse and J. Furthmüller, Phys. Rev. B **54**, 11169 (1996).

[58] P. E. Blöchl, Phys. Rev. B **50**, 17953 (1994).

[59] J. P. Perdew, K. Burke, and M. Ernzerhof, Phys. Rev. Lett. **77**, 3865 (1996).

[60] A. Togo and I. Tanaka, Scr. Mater. **108**, 1 (2015).

[61] D. Alfè, Computer Physics Communications **180**, 2622 (2009).

[62] A. T. Zayak, P. Entel, K. M. Rabe, W. A. Adeagbo, and M. Acet, Phys. Rev. B **72**, 054113 (2005).

[63] A. Zayak, W. Adeagbo, P. Entel, and K. Rabe, Appl. Phys. Lett. **88**, 111903 (2006).

[64] O. I. Velikokhatnyi and I. I. Naumov, Fiz. Tverd. Tela **41**, 684 (1999), [Physics of the Solid State **41**, 617 (1999)].

[65] Y. Lee, J. Y. Rhee, and B. N. Harmon, Phys. Rev. B **66**, 054424 (2002).

[66] C. Bungaro, K. M. Rabe, and A. Dal Corso, Phys. Rev. B **68**, 134104 (2003).

[67] C. P. Opeil, B. Mihaila, R. K. Schulze, L. Mañosa, A. Planes, W. L. Hults, R. A. Fisher, P. S. Riseborough, P. B. Littlewood, J. L. Smith, et al., Phys. Rev. Lett. **100**, 165703 (2008).

[68] T. D. Haynes, R. J. Watts, J. Laverock, Z. Major, M. A. Alam, J. W. Taylor, J. A. Duffy, and S. B. Dugdale, New J. Phys. **14**, 035020 (2012).

[69] A. Zheludev, S. M. Shapiro, P. Wochner, and L. E. Tanner, Phys. Rev. B, **54**, 15045 (1996).

[70] A. T. Zayak, P. Entel, J. Enkovaara, A. Ayuela, and R. M. Nieminen, Phys. Rev. B **68**, 132402 (2003).

[71] T. Hickel, M. A. Uijttewaal, A. Al-Zubi, B. Dutta, B. Grabowski, and J. Neugebauer, Adv. Eng. Mater. **14**, 547 (2012).

[72] R. Niemann, U. K. Rößler, M. E. Gruner, O. Heczko, L. Schultz, and S. Fähler, Adv. Eng. Mater. **14**, 562 (2012).

[73] M. E. Gruner, S. Fähler, and P. Entel, Phys. Stat. Sol. (B) **251**, 2067 (2014).

[74] M. E. Gruner, R. Niemann, P. Entel, R. Pentcheva, U. K. Rößler, K. Nielsch, and S. Fähler, Sci. Rep. **8**, 8489 (2018).

[75] K. Ullakko, J. K. Huang, C. Kantner, R. C. O'Handley, and V. V. Kokorin, Appl. Phys. Lett. **69**, 1966 (1996).

[76] A. Sozinov, A. A. Likhachev, N. Lanska, and K. Ullakko, Appl. Phys. Lett. **80**, 1746 (2002).

[77] M. Siewert, M. E. Gruner, A. Hucht, H. C. Herper, A. Dannenberg, A. Chakrabarti, N. Singh, R. Arróyave, and P. Entel, Adv. Eng. Mater. **14**, 530 (2012).

[78] P. Entel, V. D. Buchelnikov, V. V. Khovailo, A. T. Zayak, W. A. Adeagbo, M. E. Gruner, H. C. Herper, and E. F. Wassermann, J. Phys. D: Appl. Phys. **39**, 865 (2006).

[79] J. Hesse and A. Rubartsch, J. Phys. E: Sci. Instr. **7**, 526 (1974).

[80] G. L. Caer, B. Malaman, and B. Roques, Journal of Physics F: Metal Physics **8**, 323 (1978).

[81] R. A. Dunlap, R. H. March, and G. Stroink, Can. J. Phys. **59**, 1577 (1981).

[82] V. Recarte, J. I. Pérez-Landazábal, V. Sánchez-Alarcos, E. Cesari, M. Jiménez-Ruiz, K. Schmalzl, and V. A. Chernenko, Appl. Phys. Lett. **102**, 201906 (2013).

[83] S. J. Lee, Y. P. Lee, Y. H. Hyun, and Y. V. Kudryavtsev, J. Appl. Phys. **93**, 6975 (2003).

[84] M. A. Uijttewaal, T. Hickel, J. Neugebauer, M. E. Gruner, and P. Entel, Phys. Rev. Lett. **102**, 035702 (2009).

[85] P. Souvatzis, O. Eriksson, M. I. Katsnelson, and S. P. Rudin, Phys. Rev. Lett. **100**, 095901 (2008).

[86] P. Souvatzis, O. Eriksson, M. Katsnelson, and S. Rudin, Comput. Mater. Sci. **44**, 888 (2009).

[87] F. Bottin, J. Bieder, and J. Bouchet, Comput. Phys. Commun. **254**, 107301 (2020).

[88] D. M. Ceperley and B. J. Alder, Phys. Rev. Lett. **45**, 566 (1980).

[89] J. P. Perdew and A. Zunger, Phys. Rev. B **23**, 5048 (1981).

[90] J. P. Perdew, J. A. Chevary, S. H. Vosko, K. A. Jackson, M. R. Pederson, D. J. Singh, and C. Fiolhais, Phys. Rev. B **46**, 6671 (1992).